Optics Letters

Laser emission from tapered fiber-based liquid-crystal microsphere for sensing

Dong Zhou,[1] Na Zhao,[1] Yuzhou Chen,[1] Jing Sun,[1] Yuxiang Li,[1,3] Zenghui Peng,[2] and Yongjun Liu[1,2,*]

[1]Key Laboratory of In-Fiber Integrated Optics, Ministry of Education, Harbin Engineering University, Harbin 150001, China
[2]State Key Laboratory of Applied Optics, Changchun Institute of Optics, Fine Mechanics and Physics, Chinese Academy of Sciences, Changchun 130033, China
[3]liyuxiang11@hrbeu.edu.cn
*liuyj@hrbeu.edu.cn

Received 17 April 2023; revised 7 June 2023; accepted 8 June 2023; posted 9 June 2023; published 11 July 2023

This Letter introduces a novel laser emission probe for liquid-crystal microspheres based on a tapered fiber. A cholesteric liquid crystal (CLC) is injected into a hollow glass microsphere (HGM) attached at the front end of a tapered fiber in order to produce laser. Tapered fibers are preferable to rectangular fibers for liquid-crystal microsphere laser emission. The whispering gallery mode (WGM) laser is significantly suppressed by the tapered fiber-based liquid-crystal microsphere, which also displays an apparent single-mode photonic bandgap (PBG) laser peak. The stimulation response of tapered fiber-based liquid-crystal microspheres to organic vapors causes a modification of the laser peak wavelength with increasing gas concentration. In addition, laser emission generated by tapered fiber-based liquid-crystal microspheres is expected to be used in fields such as microenvironmental biosensing.

https://doi.org/10.1364/OL.492930

High-birefringence liquid-crystal materials have been popular recently. When subjected to external stimuli, these materials' physical and chemical characteristics are also changed [1]. Cholesteric liquid crystals (CLCs) are frequently employed in micro-actuators [2], smart coatings [3], electric fields [4], pH [5], and bio-detection [6] because they have representative external stimuli reactivity and biocompatibility. Fast, real-time detection of chemical gas is an emerging research field relevant to most aspects of modern society, from medical and health services to the biological microenvironment. For instance, the ketogenic diet will result in elevated levels of exhaled acetone [7] and also include biodegradation of tetrahydrofuran (THF) [8] and conversion of THF in the microenvironment [9]. A liquid crystal-based optical fiber gas sensor [10] that we proposed in earlier work still has issues, such as an unstable structure and low resolution of reflection center wavelength detection.

Organic lasers play an irreplaceable role as a new tool in several fields of the optical element. Micro-lasers are also used in many fields, such as laser displays [11] and optical switching [12]. Meanwhile, micro-lasers can also be used in cell monitoring and tracking [13] and bio-detection [14]. Liquid crystals that the director vector spontaneously twists in the direction perpendicular to the helical axis are known as chiral nematic liquid crystals. This periodic helical structure presents a one-dimensional (1D) photonic bandgap (PBG) mode to light when it is optically pumped, creating a low-threshold mirrorless laser. In a liquid environment, a Bragg microcavity is unstable [15]. To solve the problems that the instability of a Bragg microcavity causes, we propose a stable optical fiber micro-laser sensing system. The fiber probe holds great potential for applications in areas such as biotic microenvironments [16] and non-invasive disease detection [17].

In this Letter, utilizing a Y-shaped fiber branching device and hollow glass microsphere (HGM), we develop a tapered fiber-based probe for liquid-crystal microsphere laser emission. The HGM (90 μm) that is filled with CLCs that have been dye-doped is attached to the front of the tapered fiber. Due to the self-assembly of CLC within the HGM, ideal 3D Bragg microcavities are formed. When the pumping source is coupled into the fiber, the liquid-crystal microspheres on the tapered fiber probe generate 3D laser emission. The laser emission from the liquid-crystal microspheres based on the tapered fiber significantly suppresses the generation of whispering gallery mode (WGM) laser and can be utilized for the detection of organic gases.

Figure 1 displays the fabrication process of the proposed tapered 3D Bragg fiber probe. First, the multimode fiber (MMFs, from Changfei, a diameter of 125 μm, fiber core 105 μm, NA = 0.22) is heated and stretched by the electrode of the fusion splicer (FSM-80S, from Fujikura) and the tapered end is kept flat by the fiber cleaver. Second, an HGM ($n = 1.45$, $d = 90$ μm, the glass thickness is 900 nm, K25, Minnesota Mining and Manufacturing Company) is fixed to the fiber by UV curing glue (LEAFTOP 9310, from Shenzhen Tegu). Third, a micro-pore ($d \approx 15$ μm) is drilled on the surface of the HGM with a sharply tapered fiber. Finally, glycerin (from Yousuo Chemical) and dye-doped CLC (DDCLC) are injected into the HGM through a tapered microtubule (about 10 μm in diameter). The contact angle between glycerol and quartz glass surfaces is shown in

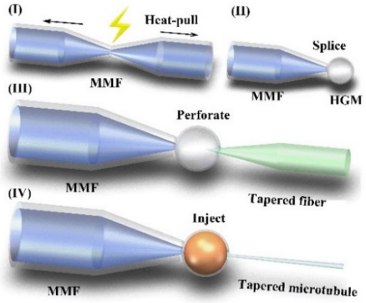

Fig. 1. Schematic diagram of microsphere tapered fiber fabrication. The fabrication process includes: (I) tapered fiber drawing, (II) fixation of HGMs, (III) glass microsphere perforation, and (IV) injected liquid crystal.

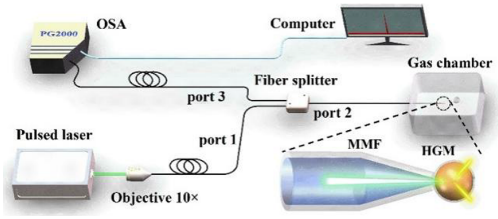

Fig. 2. Schematic of the experimental system.

Fig. S1 in Supplement 1. Glycerol exhibits hydrophilicity and diffusion properties on the surface of quartz glass, allowing it to rapidly wet the inner wall of the HGM. The diameter of the microtubule must be smaller than the diameter of the HGM micro-pore, which facilitates the exhaust of air (see Figs. S2 and S3 in Supplement 1). The glycerin is used as an alignment agent and the volume of the glycerin occupies 10% of the HGM. By adding 2.6 wt% of the R5011 [helical twisting power (HTP) is ~115 μm^{-1}] chiral agent to the nematic liquid crystal (E7, from Chengzhi Yonghua, $n_e = 1.692$, $n_o = 1.522$, $Cp = 61°C$, $Mp = -10°C$) and ultrasonically shaking them for 10 mins at 80°C, the CLC1 is produced. Laser dye 4-dicyano-methylene-2-methyl- (6–4-dimethylaminostryl)-4H-pyan (DCM, from Exciton) with a concentration of 1 wt% is added into CLC as the gain medium. According to the principle of Bragg reflection, the reflection band center is $\lambda_c = \bar{n} \cdot p$ [18], where $\bar{n}$ is the average refractive index of liquid crystal, $p = 1/(HTP \cdot c)$ is the helical pitch, and c is the concentration of the chiral dopant. The positions of the edges of the reflection band wavelength are $\lambda_e = n_e p$ and $\lambda_o = n_o p$, respectively.

Figure 2 shows the schematic diagram of the experimental system. The pumping source uses a frequency-doubled Nd:YAG pulsed laser ($\lambda = 532$ nm, pulse duration 8 ns, and repetition rate 5 Hz). The pump laser is passed through the objective (10×) and coupled into a Y-shaped fiber branching device (port 1). The output ends of the optical fiber branching device are connected to the fiber probe (port 2) located in the gas chamber (400 mL). The spectrum signals of excited DDCLC are collected via port 3 and transmitted to a high-speed optical spectrum analyzer (OSA, PG2000, Ideaoptics, the spectral resolution is 0.04 nm).

When a trace amount of glycerol is added to the HGM, DDCLC can self-assemble into a radially periodic structure of 3D Bragg microcavities in a short time [19]. The wavelength of the laser emission corresponds to the reflection band edge of CLC, which can be tuned by shifting the reflection band within the fluorescence emission spectral range of the laser dye.

During the cone extension, although the hot glass is assumed to be soft enough and stretchable, it is not so soft that it sags due to the cone's own weight. The toughness of the glass outside the electrically heated area allows the tapered ends to be extended steadily. The taper profile function [$r(z)$] can be defined mathematically based on the conservation of mass and volume of the tapered stretch [20], i.e.:

$$r(z) = r_0 \exp[-\frac{1}{2}\int_0^x \frac{dx}{L(x)}] \cdot x(z), \tag{1}$$

$$z(x) = \frac{1}{2}[x + L_0 - L(x)], \tag{2}$$

where r_0 is the radius of the fiber before fused biconical taper. z is the longitudinal coordinate along the fiber and x is the extension distance of the point z being pulled out of the heated area. $z(x)$ is the tapered transition length as x, and $L(x)$ is the variation curve of the fiber length in the heated region with taper extension. Invert Eq. (2) to obtain $x(z)$, then substitute $x(z)$ into Eq. (1) to get the tapered fiber profile function.

For boosting and improving the excitation properties of the liquid-crystal microsphere, the transmission property of the tapered fiber is crucial. During the stretching of the standard to tapered fiber, the proportion of cladding to the core practically stays the same [21]. Using the finite-difference beam propagation approach, the Gaussian energy distribution of several types of fiber transmission to the microsphere (dashed section) is shown in Fig. 3. The Gaussian beam [22] in the fiber is given by

$$I(\theta_i) = I_0 \exp[-tan^2\theta_i / tan^2\theta_i^{max}]. \tag{3}$$

I_0 is the pump source energy and θ_i is the angle of incidence of the beam at the fiber end. The fiber cladding and core have refractive indices of 1.444 and 1.452, respectively. The fiber has a 125-μm diameter and a 105-μm core. The energy distribution of a rectangular fiber without any processing is shown in Fig. 3(a), where it is transmitted along the fiber and radiated at the fiber end to the air medium ($n = 1$). The energy transmission of the tapered fiber in the power function model is depicted in Fig. 3(b). This fiber has high energy at its end and a small energy loss at the waist portion of the taper. The energy radiated at the end of the fiber is eventually parallel and scattered. Figure 3(c) shows the energy transmission diagram of the exponential function model tapered fiber, where the energy is more concentrated compared to Fig. 3(b). The majority of the energy that eventually radiates from the fiber end is, however, also scattered and challenging to manufacture. The linear function model of tapered fiber energy transmission is shown in Fig. 3(d). With the exception of a small amount of energy divergence, the majority of the energy converges into the core of the microsphere, generating an extremely strong pumping energy to excite the PBG mode. Since the tapered fiber has a strong field enhancement effect in the tapered waist part, the simulation's Gaussian light source is less energetic to better observe the tapered fiber's energy distribution and prevent energy saturation.

Figure 4(a) shows the effect of the rectangular and tapered structure of the fiber on the laser emission and the inset shows microscopic images of two optical fiber structures. The dashed bright spots refer to the artifact of microscopic illumination. The same pump energy and frequency enable both structures to excite the PBG laser. However, the rectangular fiber without

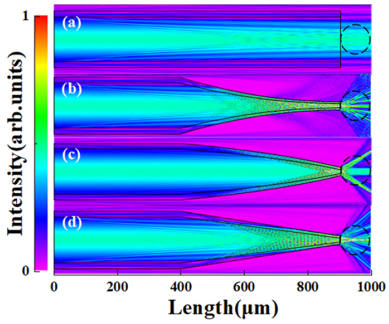

Fig. 3. Simulation of the fiber energy distribution for the (a) rectangular optical fiber, (b) quadratic function model, (c) exponential function model, and (d) linear function model. The dotted line shows the position of the liquid-crystal microsphere at the fiber end.

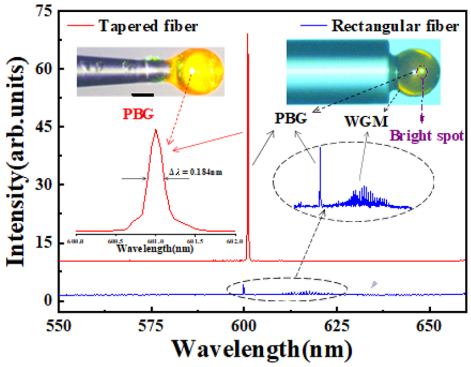

Fig. 4. Comparison of laser emission spectra of liquid-crystal microspheres in rectangular and tapered fibers. Inset: larger version of laser spectra of rectangular fiber and tapered fiber liquid-crystal microsphere. Scale bar: 50 μm.

any treatment can excite the WGM laser. After magnifying the emission spectrum based on the tapered fiber structure, no clear WGM signal was found (see Fig. S4 in Supplement 1). The reason for this phenomenon is that the energy in the fiber does not converge. Part of the energy in the fiber core goes to the center of the microsphere for excitation of the PBG mode, and another part of the energy goes to the edge of the microsphere for excitation of the WGM. The tapered fiber converges the energy so that the liquid-crystal microspheres excite a stronger single-mode laser. The tapered fiber-based DDCLC laser emission threshold is 1.82 μJ/mm^2 (see Fig. S5 in Supplement 1). The bandwidth of the laser peak is only 0.184 nm. Figure S6 in Supplement 1 presents a comparison of laser emission spectra under two conditions: with and without the addition of glycerol. In the absence of a glycerol alignment layer in the HGM, the quality of laser emission spectra is diminished. From 27°C to 41°C, the PBG laser at the longer wavelength edge of the reflection band exhibited a blueshift of 10.5 nm (see Fig. S7 in Supplement 1). The temperature-dependent reflection spectra of CLC1 are shown in Fig. S8 in Supplement 1. The spectra demonstrate a lower sensitivity to the temperature at the shorter wavelength edge of the reflection band and a minimal redshift. Simultaneously, the sensitivity of the PBG laser at the short-wavelength edge toward organic vapors is reduced. According to $\lambda_e = n_e p$, the pitch/temperature

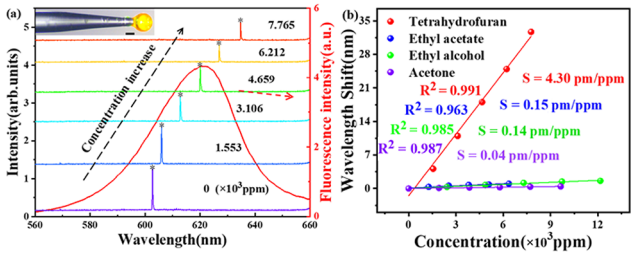

Fig. 5. (a) Laser emission spectra with increasing THF concentration. Inset: laser gain micrograph of liquid-crystal microspheres based on tapered fiber. (b) Correlation of the response of liquid crystals to different organic vapors. Scale bar: 50 μm.

dependence (∂P/∂T) is as follows [23]:

$$\frac{\partial \mathrm{P}}{\partial \mathrm{T}} = -\frac{1}{\beta} - \frac{3T_c\left(1-\frac{T}{T_c}\right)^{1-\beta}}{2\Delta n \cdot \beta} \cdot \frac{\partial \lambda_e}{\partial \mathrm{T}}, \tag{4}$$

where the parameters of Δn and β are influenced by wavelength and are independent of temperature. In Eq. (4), Δn is the liquid-crystal birefringence in the crystalline state, the exponent β is a material constant, and T_c is the clearing temperature of the liquid-crystal material under investigation.

We placed the fiber probe in a gas chamber and detected the response of liquid crystals to different types of organic vapors using a titration method. Figure 5 presents the response of the tapered fiber-based liquid-crystal microsphere to different organic vapors. Figure 5(a) shows the spectral response of CLC1 to different THF concentrations. The spectra show a noticeable redshift, which is caused by the weakened interaction between the liquid-crystal molecules brought on by the gas, which also causes an increase in the pre-inclination angle and the pitch [24]. The location of the dye's best gain also affects where the laser peak appears [25]. The liquid-crystal laser experiences its greatest gain between 590 and 650 nm, as shown by the red line, which also shows the emission wavelength range and intensity of the DCM fluorescent dye. A micrograph of laser emission from a liquid-crystal microsphere built on a tapered fiber is shown in the inset. This image reveals a liquid-crystal microcavity that has experienced high gain, resulting in brilliant spots. Figure 5(b) presents the response of CLC1 to different types of organic vapors. The CLC1 responds very little to organic vapors other than THF. The cause of this may be related to the dipole moments of different organic solvent molecules [26]. Gas molecules with smaller dipole moments are more easily adsorbed by liquid crystals. Additionally, the difference in solubility of different organic vapors in CLC1 is also a contributing factor to this result. Higher concentrations of THF disrupt the alignment of liquid-crystal molecules within DDCLC, resulting in the inability to generate laser emission (see Fig. S9 in Supplement 1). The maximum sensitivity is 4.3 pm/ppm and the minimum sensitivity is 0.04 pm/ppm.

Another important factor for identifying gas concentrations is stability. Figure 6 presents the temporal stability of laser emission from a tapered fiber-based liquid-crystal microsphere. The wavelength stability of the laser emission from the liquid-crystal microsphere under the continuous operation of the pump source for 10 mins at a frequency of 5 Hz is depicted in Fig. 6(a). Under the absence of temperature and organic vapor influence, the laser emission wavelength remains stable at 602 nm. During laser

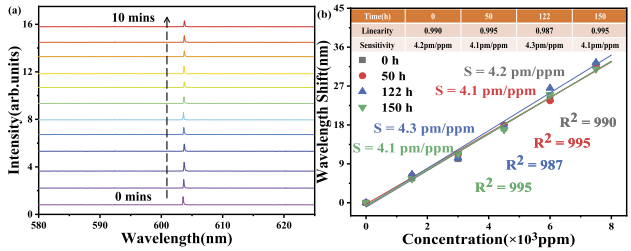

Fig. 6. (a) Stability of laser emission wavelength over time when unaffected by temperature and organic vapor. (b) Sensitivity of THF concentration measured at different times.

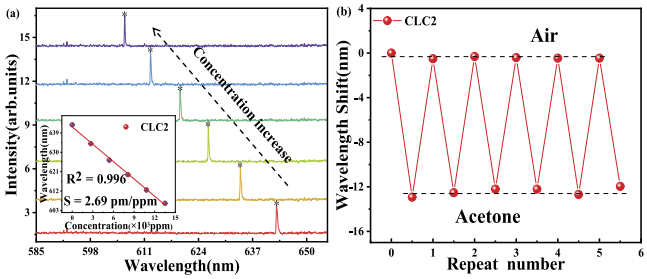

Fig. 7. (a) Spectrogram of CLC2 with increasing acetone concentration. Inset: acetone concentration as a function of wavelength. (b) Repeatability of the CLC2 response to acetone.

pumping, the internal temperature of the liquid-crystal microsphere is minimally affected, and the laser emission wavelength of the liquid-crystal microsphere remains stable without any shifts. Figure 6(b) depicts the same liquid-crystal microsphere with multiple measurements of the THF concentration made within 150 h. Over this period, the data demonstrate good detection performance. Small variations in the amount of THF solvent introduced into the gas chamber each time and cumulative discrepancies in the selection of data points cause differences in the sensitivity of the linear fits.

Acetone is a very flammable organic solvent that impairs air quality. In addition, acetone in the breath may also be a useful indicator of diabetes [27]. E7 was made into CLC2 by adding 25 wt% of the chiral agent R811. The preparation method was as above. Figure 7(a) displays the spectrogram of the CLC2 responsiveness to acetone at 31°C. Due to the tilt of the liquid-crystal helical axis, elastic constants, drop in refractive index, and π–π bond stacking, the spectrum shows a significant blueshift with increasing acetone concentration [24]. The plot of CLC2 laser emission wavelength against acetone concentration can be seen in the inset. The statistical results of multiple measurements show that acetone had a stimulatory response to CLC2 with a sensitivity of 2.69 pm/ppm. To prevent leakage of acetone gas during the data collection process in repetitive experiments, we placed seven chambers in a water bath constant temperature system. Among them, six chambers were titrated with the same concentration of acetone, while the remaining chamber did not contain any organic vapor. The repetitive results of CLC2's response to organic vapor were measured using the same tapered fiber probe, as shown in Fig. 7(b).

In conclusion, this Letter describes a novel fiber probe that induces 3D laser emission from a liquid-crystal microsphere at the tapered fiber end. Strong PBG mode laser is easily recognized because the CLC molecules in the liquid-crystal microsphere self-assemble to create a flawless Bragg cavity. Additionally, as the concentration of organic vapor rises, so does the wavelength of the PBG laser peak produced by the ultra-compact, stable structure and performance fiber probe. The sensibility of the same liquid crystal to different organic gases varies. The sensitivity of CLC1 to THF was 4.3 pm/ppm and to acetone was only 0.04 pm/ppm, while the sensitivity of CLC2 to acetone was –2.96 pm/ppm. The probe also has a better potential for non-invasive detection applications because acetone in breath may be a helpful predictor of diabetes.

Disclosures. The authors declare no conflicts of interest.

Data availability. Data underlying the results presented in this paper are not publicly available at this time but may be obtained from the authors upon reasonable request.

Supplemental document. See Supplement 1 for supporting content.

REFERENCES

1. C. Kaspar, B. J. Ravoo, W. G. van der Wiel, S. V. Wegner, and W. H. P. Pernice, Nature **594**, 345 (2021).
2. M. Y. Yang, Y. Y. Xu, X. Zhang, H. K. Bisoyi, P. Xue, Y. Z. Yang, X. Yang, C. Valenzuela, Y. H. Chen, L. Wang, W. Feng, and Q. Li, Adv. Funct. Mater. **32**, 2201884 (2022).
3. D. C. Hoekstra, B. van der Lubbe, T. Bus, L. T. Yang, N. Grossiord, M. G. Debije, and A. Schenning, Angew. Chem., Int. Ed. **60**, 10935 (2021).
4. M. Humar, Liq. Cryst **43**, 1937 (2016).
5. Y. Wang, L. Y. Zhao, A. J. Xu, L. Wang, L. L. Zhang, S. Q. Liu, Y. J. Liu, and H. Y. Li, Sens. Actuators, B **258**, 1090 (2018).
6. C. L. Xia, D. Zhou, Y. M. Su, G. K. Zhou, L. S. Yao, W. M. Sun, and Y. J. Liu, Analyst **145**, 5951 (2020).
7. L. R. Saslow, S. Kim, J. J. Daubenmier, J. T. Moskowitz, S. D. Phinney, V. Goldman, E. J. Murphy, R. M. Cox, P. Moran, and F. M. Hecht, PLoS One **9**, e91027 (2014).
8. H. Masuda, K. McClay, R. J. Steffan, and G. J. Zylstra, J. Mol. Microbiol. Biotechnol. **22**, 312 (2012).
9. W. J. Shi, L. Y. Cao, H. Zhang, X. Zhou, B. An, Z. K. Lin, R. H. Dai, J. F. Li, C. Wang, and W. B. Lin, Angew. Chem., Int. Ed. **56**, 9704 (2017).
10. Y. H. Yang, D. Zhou, X. J. Liu, Y. J. Liu, S. Q. Liu, P. X. Miao, Y. C. Shi, and W. M. Sun, Opt. Express **28**, 31872 (2020).
11. J. Y. Zhao, Y. L. Yan, Z. H. Gao, Y. X. Du, H. Y. Dong, J. N. Yao, and Y. S. Zhao, Nat. Commun. **10**, 870 (2019).
12. Z. H. Gao, W. Zhang, Y. L. Yan, J. Yi, H. Y. Dong, K. Wang, J. N. A. Yao, and Y. S. Zhao, ACS Nano **12**, 5734 (2018).
13. Z. Lv, Z. W. Man, Z. Z. Xu, C. F. Feng, Y. Yang, Q. Liao, X. Wang, L. M. Zheng, and H. B. Fu, ACS Appl. Mater. Interfaces **10**, 32981 (2018).
14. Z. R. Xiong, H. Zhang, Y. L. Lu, L. L. Zhang, W. M. Sun, and Y. J. Liu, IEEE Sens. J. **20**, 617 (2020).
15. M. Humar and I. Musevic, Opt. Express **18**, 26995 (2010).
16. C. Boesch-Saadatmandi, G. Rimbach, A. Jungblut, and J. Frank, Cytotechnology **63**, 89 (2011).
17. C. Course, W. J. Watkins, C. Muller, D. Odd, S. Kotecha, and M. Chakraborty, J. Breath Res. **15**, 024002 (2021).
18. Y. Zhou, Y. Huang, and S. T. Wu, Opt. Express **14**, 3906 (2006).
19. F. Xu and P. P. Crooker, Phys. Rev. E **56**, 6853 (1997).
20. T. A. Birks and Y. W. Li, J. Lightwave Technol. **10**, 432 (1992).
21. R. P. Kenny, T. A. B. and K, and P. Oakley, Electron. Lett. **27**, 1654 (1991).
22. Y. X. Zhang, X. Y. Pu, K. Zhu, and L. Feng, J. Opt. Soc. Am. B **28**, 2048 (2011).
23. M. Ma, S. G. Li, X. L. Jing, and H. L. Chen, Opt. Eng. **56**, 1 (2017).
24. K. J. Kek, J. J. Z. Lee, Y. Otono, and S. Ishihara, J. Soc. Inf. Disp. **25**, 366 (2017).
25. J. Liu, Y. J. Chen, F. Jin, J. X. Wang, T. Ikeda, and L. Jiang, Adv. Mater. **34**, 2108330 (2022).
26. B. Gurboga and E. Kemiklioglu, Liq. Cryst. **49**, 1428 (2022).
27. A. Staerz, I. Boehme, D. Degler, M. Bahri, D. E. Doronkin, A. Zimina, H. Brinkmann, S. Herrmann, B. Junker, O. Ersen, J. D. Grunwaldt, U. Weimar, and N. Barsan, Nanomaterials **8**, 892 (2018).